3D simulation of wind turbine rotors at full scale. Part II: Fluid-structure interaction modeling with composite blades

Y. Bazilevs[a,*], M.-C. Hsu[a], J. Kiendl[b], R. Wüchner[b], K.-U. Bletzinger[b]

[a]*Department of Structural Engineering, University of California, San Diego, 9500 Gilman Drive, La Jolla, CA 92093, USA*
[b]*Lehrstuhl für Statik, Technische Universität München, Arcisstrasse 21, 80333 München, Germany*

Abstract

In this two-part article we present a collection of numerical methods combined into a single framework, which has the potential for a successful application to wind turbine rotor modeling and simulation. In Part 1 of this article we focus on: 1. The basics of geometry modeling and analysis-suitable geometry construction for wind turbine rotors; 2. The fluid mechanics formulation and its suitability and accuracy for rotating turbulent flows; 3. The coupling of air flow and a rotating rigid body. In Part 2 we focus on the structural discretization for wind turbine blades and the details of the fluid–structure interaction computational procedures. The methods developed are applied to the simulation of the NREL 5MW offshore baseline wind turbine rotor. The simulations are performed at realistic wind velocity and rotor speed conditions and at full spatial scale. Validation against published data is presented and possibilities of the newly developed computational framework are illustrated on several examples.

Keywords: wind turbine rotor, wind turbine blades, fluid–structure interaction, Kirchhoff-Love shells, composite materials, isogeometric analysis, NURBS, aerodynamic torque

1. Introduction

Coupled fluid-structure interaction (FSI) simulations at full scale are essential for accurate modeling of wind turbines. The motion and deformation of the wind turbine blades depend on the wind speed and air flow, and the air flow patterns depend on the motion and deformation of the blades. In recent years, standalone 3D fluid mechanics simulations with simplified wind turbine configurations were reported in [1–4], some at reduced scale and some with limitations in terms of the

*Corresponding author
Email address: yuri@ucsd.edu (Y. Bazilevs)

representation of the exact geometry and prediction of the FSI involved. Structural analyses of the individual turbine blades under assumed load conditions or loads coming from separate computational fluid dynamics simulations were also reported (see, e.g. [5–8]). To the best of our knowledge, no coupled fluid-structure simulations of the full-scale wind turbine blades were attempted. This problem presents a significant computational challenge because of the high wind speeds, complex and sharp geometric features, and sizes of the wind turbines under consideration. This in part explains the current, modest nature of the state-of-the-art in wind turbine simulation. In order to simulate the coupled problem, the equations governing the air flow and the blade motions and deformations need to be solved simultaneously, with proper kinematic and dynamic conditions coupling the two physical systems. Without that the modeling cannot be realistic.

In this work, we use isogeometric analysis based on Non-Uniform Rational B-Splines (NURBS) [9] for FSI modeling of wind turbine rotors. In Part 1 [10] of this article the wind turbine geometry modeling and aerodynamics simulation procedures were described in detail and the validation results were presented. In this work, we focus on the details of structural and FSI modeling.

The blade structure is governed by the isogeometric rotation-free shell formulation with the aid of the bending strip method [11]. The method is appropriate for thin shell structures comprised of multiple C^1- or higher-order continuous surface patches that are joined or merged with continuity no greater than C^0. The Kirchhoff-Love shell theory that relies on higher-order continuity of the basis functions is employed in the patch interior as in [12]. Strips of fictitious material with unidirectional bending stiffness and with zero mass and membrane stiffness are added at patch interfaces in the overlapping fashion. The direction of bending stiffness is chosen to be transverse to the patch interface. This choice leads to an approximate satisfaction of the appropriate kinematic constraints at patch interfaces without introducing additional stiffness to the shell structure. Furthermore, as the functional representation of the structural patches is enriched, the thickness of the overlap region goes to zero. Although NURBS-based isogeometric analysis is employed in this work, other discretizations such as T-Splines [13, 14] or Subdivision surfaces [15–17] are perfectly suited for the proposed structural modeling methodology.

The FSI formulation presented in this paper assumes matching discretization at the fluid-structure interface. We adopt a strongly-coupled solution strategy and employ Newton linearization to solve the nonlinear coupled equations for the fluid, structure and fluid mesh motion. However, the fluid, structure, and mesh linear solves are decoupled at the Newton iteration level, leading to a block-iterative FSI procedure [18]. The approach is robust due to the relatively large rotor mass. We note that the lack of rotational degrees of freedom in the structural discretization facilitates the strong FSI coupling.

The paper is outlined as follows. In Section 2 we describe the individual constituents of the FSI problem. We recall the air modeling approach from Part 1 of this paper. We give details of the structural formulation for wind turbine blades that

is based on the bending strip method. We also briefly describe our composite material modeling procedures for wind turbine blades. We then focus on the problem of the fluid domain motion. We develop a formulation in which the rotating part of the fluid domain motion is handled exactly, while the rest is computed using elastostatics. We conclude the section with a statement of a fully-coupled FSI problem. In Section 3 we present our discrete solution procedures for the coupled FSI problem. We also introduce a new class of time integration procedures for structures dominated by large rotational motions. In Section 4 we simulate the NREL 5MW offshore baseline wind turbine rotor [19] and present the computational results. In Section 5 we draw conclusions and outline future research directions.

2. Fluid-structure interaction modeling

In this section we present the coupled fluid-structure interaction (FSI) formulation with an emphasis on wind turbine rotors.

2.1. Air flow modeling

Air flow modeling, governed by the Navier-Stokes equations of incompressible flow in the arbitrary Lagrangian-Eulerian (ALE) form, is described in detail in Part 1 [10] of this article. Here we restate the weak formulation of the Navier-Stokes equations for completeness. We introduced a slight change in the notation to facilitate the presentation of the FSI problem.

Let $\mathcal{V}^f$ and $\mathcal{W}^f$ be the standard solution and weighting function spaces for the fluid problem. We seek the velocity-pressure pair $\{\boldsymbol{v}, p\} \in \mathcal{V}^f$, such that for all weighting functions $\{\boldsymbol{w}^f, q^f\} \in \mathcal{W}^f$,

$$B^f\left(\{\boldsymbol{w}^f, q^f\}, \{\boldsymbol{v}, p\}; \boldsymbol{v}^m\right) - F^f\left(\{\boldsymbol{w}^f, q^f\}\right) = 0, \tag{1}$$

where

$$\begin{aligned} B^f\left(\{\boldsymbol{w}^f, q^f\}, \{\boldsymbol{v}, p\}; \boldsymbol{v}^m\right) = &\left(\boldsymbol{w}^f,\, \rho^f \frac{\partial \boldsymbol{v}}{\partial t}\right)_{\Omega_t^f} + \left(\boldsymbol{w}^f,\, \rho^f\left(\boldsymbol{v} - \boldsymbol{v}^m\right) \cdot \nabla_x \boldsymbol{v}\right)_{\Omega_t^f} + \left(q^f,\, \nabla_x \cdot \boldsymbol{v}\right)_{\Omega_t^f} \\ &- \left(\nabla_x \cdot \boldsymbol{w}^f,\, p\right)_{\Omega_t^f} + \left(\nabla_x^s \boldsymbol{w}^f,\, 2\mu^f \nabla_x^s \boldsymbol{v}\right)_{\Omega_t^f}, \end{aligned} \tag{2}$$

and

$$F^f\left(\{\boldsymbol{w}^f, q^f\}\right) = \left(\boldsymbol{w}^f,\, \rho^f \boldsymbol{f}^f\right)_{\Omega_t^f} + \left(\boldsymbol{w}^f,\, \boldsymbol{h}^f\right)_{\Gamma_t^{f,N}}. \tag{3}$$

In the above equations, $\boldsymbol{v}^m$ is the fluid domain velocity, μ^f is the dynamic viscosity, ρ^f is the density, $\boldsymbol{h}^f$ is the boundary traction vector, and $\boldsymbol{f}^f$ is the body force per unit mass. Ω_t^f is the fluid domain in the current configuration, $\Gamma_t^{f,N}$ is the Neumann part of the fluid domain boundary, ∇_x is the gradient operator on Ω_t^f, ∇_x^s is its symmetrization, and $(\cdot,\cdot)_D$ denotes the usual L^2-inner product over D. The variational equations (1)-(3) represent the balance of mass and linear momentum for the incompressible fluid.

2.2. Structural modeling of the wind turbine blades

The bending strip method is used for rotation-free thin shell analysis of the wind turbine blades. The method was first proposed and applied to the solution of elastostatic problems in [11]. In this work, the bending strip methodology is extended to simulate dynamic phenomena. To present the variational equations governing the motion of the structure, we first define

$$\Omega_0^s = \bigcup_{i=1}^{N_{sp}} \Omega_{0\,i}^s, \tag{4}$$

$$\Omega^s = \bigcup_{i=1}^{N_{sp}} \Omega_i^s, \tag{5}$$

$$\Omega_0^b = \bigcup_{i=1}^{N_{bp}} \Omega_{0\,i}^b, \tag{6}$$

$$\Omega^b = \bigcup_{i=1}^{N_{bp}} \Omega_i^b. \tag{7}$$

Ω_0^s and Ω^s denote the structure midsurface in the reference and deformed configuration, respectively. $\Omega_{0\,i}^s$ and Ω_i^s, $i = 1, 2, \ldots, N_{sp}$, are the structural patches or subdomains in the reference and deformed configuration, respectively, and N_{sp} is their number. $\Omega_{0\,i}^b$ and Ω_i^b, $i = 1, 2, \ldots, N_{bp}$, are the bending strip patches in the reference and deformed configuration, respectively, and N_{bp} is their number.

We define the following inner products of arbitrary functions f and g, taken patch-wise, as

$$(f, g)_{\Omega_0^s} = \sum_{i=1}^{N_{sp}} \int_{\Omega_{0\,i}^s} f g \, d\Omega_0^s, \tag{8}$$

$$(f, g)_{\Omega^s} = \sum_{i=1}^{N_{sp}} \int_{\Omega_i^s} f g \, d\Omega^s, \tag{9}$$

$$(f, g)_{\Omega_0^b} = \sum_{i=1}^{N_{bp}} \int_{\Omega_{0\,i}^b} f g \, d\Omega_0^b, \tag{10}$$

$$(f, g)_{\Omega^b} = \sum_{i=1}^{N_{bp}} \int_{\Omega_i^b} f g \, d\Omega^b. \tag{11}$$

Let $\mathcal{V}^s$ and $\mathcal{W}^s$ denote the trial solution and weighting function spaces for the structural problem. We seek the displacement of the shell midsurface $\boldsymbol{u} \in \mathcal{V}^s$, such that for all weighting functions $\boldsymbol{w}^s \in \mathcal{W}^s$,

$$B^s(\boldsymbol{w}^s, \boldsymbol{u}) - F^s(\boldsymbol{w}^s) = 0, \tag{12}$$

where

$$B^s(\boldsymbol{w}^s, \boldsymbol{u}) = \left(\boldsymbol{w}^s,\, \rho_0^s h \frac{\partial^2 \boldsymbol{u}}{\partial t^2}\right)_{\Omega_0^s} + \left(\delta\boldsymbol{\varepsilon}(\boldsymbol{u})[\boldsymbol{w}^s],\, \mathbf{A}(h)\boldsymbol{\varepsilon}(\boldsymbol{u}) + \mathbf{B}(h)\boldsymbol{\kappa}(\boldsymbol{u})\right)_{\Omega_0^s} + \left(\delta\boldsymbol{\kappa}(\boldsymbol{u})[\boldsymbol{w}^s],\, \mathbf{B}(h)\boldsymbol{\varepsilon}(\boldsymbol{u}) + \mathbf{D}(h)\boldsymbol{\kappa}(\boldsymbol{u})\right)_{\Omega_0^s} + \left(\delta\boldsymbol{\kappa}(\boldsymbol{u})[\boldsymbol{w}^s],\, \frac{h^3}{12}\mathbf{C}^b\boldsymbol{\kappa}(\boldsymbol{u})\right)_{\Omega_0^b}, \tag{13}$$

and

$$F^s(\boldsymbol{w}^s) = (\boldsymbol{w}^s,\, \rho^s h \boldsymbol{f}^s)_{\Omega^s} + (\boldsymbol{w}^s,\, \boldsymbol{h}^s)_{\Omega^s}\,. \tag{14}$$

In the above, ρ_0^s and ρ^s are the structural mass densities in the reference and deformed configuration, respectively, h is the shell thickness, $\boldsymbol{f}^s$ is the body force (e.g. gravity), and $\boldsymbol{h}^s$ is the prescribed surface traction. $\mathbf{A}$, $\mathbf{B}$ and $\mathbf{D}$ are the extensional (membrane), coupling and bending material stiffness tensors, respectively, pre-integrated through the shell thickness, and $\boldsymbol{\varepsilon}$ and $\boldsymbol{\kappa}$ are the membrane strains and changes in curvature, respectively (see [12] for details). Their first variations, $\delta\boldsymbol{\varepsilon}(\boldsymbol{u})[\boldsymbol{w}^s]$ and $\delta\boldsymbol{\kappa}(\boldsymbol{u})[\boldsymbol{w}^s]$, are given by

$$\delta\boldsymbol{\varepsilon}(\boldsymbol{u})[\boldsymbol{w}^s] = \frac{d}{d\epsilon}\boldsymbol{\varepsilon}(\boldsymbol{u} + \epsilon\boldsymbol{w}^s)\bigg|_{\epsilon=0}, \tag{15}$$

$$\delta\boldsymbol{\kappa}(\boldsymbol{u})[\boldsymbol{w}^s] = \frac{d}{d\epsilon}\boldsymbol{\kappa}(\boldsymbol{u} + \epsilon\boldsymbol{w}^s)\bigg|_{\epsilon=0}, \tag{16}$$

where ϵ is a real number. Equations (12)-(14) represent the balance of linear momentum for the structure. It is assumed in Eq. (13) that the linear stress-strain relationship for the structure holds (i.e. the St.Venant-Kirchhoff model). Despite the linear stress-strain relationship, the structural formulation is objective and thus applicable to large deformation problems.

In Eq. (13), $\mathbf{C}^b$ is the constitutive material matrix for the bending strip patches. In the local Cartesian coordinate system oriented on the tangent vector orthogonal to the patch interface, $\mathbf{C}^b$ may be expressed in Voigt notation as

$$\mathbf{C}^b = \begin{bmatrix} E_s & 0 & 0 \\ 0 & 0 & 0 \\ 0 & 0 & 0 \end{bmatrix}, \tag{17}$$

where E_s is the bending strip modulus of elasticity. The bending strip constitutive matrix is designed to ensure that no extra stiffness is added to the structure and the bending moment is appropriately transferred between the structural patches. E_s scales linearly with the structural stiffness and, provided it is large enough, has little influence on the structural response (see [11]).

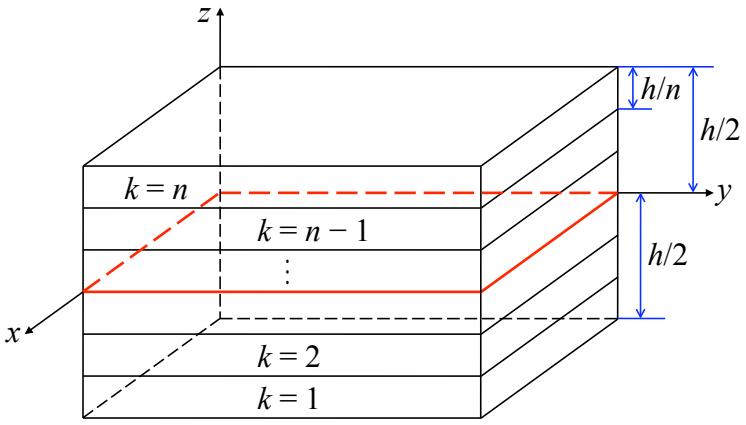

Figure 1: Schematic of a composite laminate.

2.2.1. Composite shell modeling

Composite materials are used in modern wind turbine blade designs to reduce the rotor mass (and production costs) and at the same time give it the necessary stiffness to withstand operational loads. In what follows, we present our composite modeling procedures for wind turbine blades.

We use the classical laminated plate theory [20] and homogenize the material through-thickness constitutive behavior for a given composite ply layout. Let k denotes the k^{th} ply (or lamina) and let n be the total number of plies (see Figure 1). We assume each ply has the same thickness h/n. Pre-integrating through the thickness, the extensional stiffness $\mathbf{A}$, coupling stiffness $\mathbf{B}$ and bending stiffness $\mathbf{D}$ in Eq. (13) are given by

$$\mathbf{A}(h) = \int_{-\frac{h}{2}}^{\frac{h}{2}} \overline{\mathbf{C}}(z)dz = \frac{h}{n}\sum_{k=1}^{n} \overline{\mathbf{C}}_k, \tag{18}$$

$$\mathbf{B}(h) = \int_{-\frac{h}{2}}^{\frac{h}{2}} \overline{\mathbf{C}}(z)z dz = \frac{h^2}{n^2}\sum_{k=1}^{n} \overline{\mathbf{C}}_k \left(k - \frac{n}{2} - \frac{1}{2}\right), \tag{19}$$

$$\mathbf{D}(h) = \int_{-\frac{h}{2}}^{\frac{h}{2}} \overline{\mathbf{C}}(z)z^2 dz = \frac{h^3}{n^3}\sum_{k=1}^{n} \overline{\mathbf{C}}_k \left[\left(k - \frac{n}{2} - \frac{1}{2}\right)^2 + \frac{1}{12}\right], \tag{20}$$

where

$$\overline{\mathbf{C}}_k = \boldsymbol{T}^T(\phi_k)\,\mathbf{C}\,\boldsymbol{T}(\phi_k), \tag{21}$$

$$\mathbf{C} = \begin{bmatrix} \dfrac{E_1}{(1-\nu_{12}\nu_{21})} & \dfrac{\nu_{21}E_1}{(1-\nu_{12}\nu_{21})} & 0 \\ \dfrac{\nu_{12}E_2}{(1-\nu_{12}\nu_{21})} & \dfrac{E_2}{(1-\nu_{12}\nu_{21})} & 0 \\ 0 & 0 & G_{12} \end{bmatrix}, \tag{22}$$

$$\boldsymbol{T}(\phi) = \begin{bmatrix} \cos^2\phi & \sin^2\phi & \sin\phi\cos\phi \\ \sin^2\phi & \cos^2\phi & -\sin\phi\cos\phi \\ -2\sin\phi\cos\phi & 2\sin\phi\cos\phi & \cos^2\phi - \sin^2\phi \end{bmatrix}. \tag{23}$$

In the above equations, ϕ is the fiber orientation angle in each ply, E_1 and E_2 are the Young's moduli of the unidirectional lamina, ν's are the Poisson ratios, G_{12} is the shear modulus, and $\nu_{21}E_1 = \nu_{12}E_2$ to ensure the symmetry of the constitutive material matrix $\mathbf{C}$. Equation (21) transforms $\mathbf{C}$ from the principal material coordinates to the laminate coordinates (i.e. the local Cartesian basis defined in [11]) for each ply and $\overline{\mathbf{C}}_k$ is constant within each ply.

Remark: Setting $n = 1$ and $\overline{\mathbf{C}}_k = \mathbf{C}$ in Eqs. (18)-(20), we get $\mathbf{B}(h) = \mathbf{0}$ and

$$\mathbf{A}(h) = h\mathbf{C}, \tag{24}$$

$$\mathbf{D}(h) = \frac{h^3}{12}\mathbf{C}, \tag{25}$$

which are the classical membrane and bending stiffnesses for the orthotropic shell.

2.2.2. Decomposition of the structural displacement into rotation and deflection

In the case of wind turbine rotors, the structural motions are dominated by the rotation. As a result, it is useful to decompose the structural displacement $\boldsymbol{u}$ into its rotation and deflection components as

$$\boldsymbol{u} = \boldsymbol{u}_\theta + \boldsymbol{u}_d. \tag{26}$$

The rotational component of the displacement may be computed as

$$\boldsymbol{u}_\theta = (\boldsymbol{R}(\theta) - \boldsymbol{I})\,(\boldsymbol{X} - \boldsymbol{X}_0)\,, \tag{27}$$

where $\boldsymbol{X}$ are the coordinates of the structure reference configuration, $\boldsymbol{X}_0$ is a fixed point, θ is the time-dependent angle of rotation, $\boldsymbol{R}(\theta)$ is the rotation matrix and $\boldsymbol{I}$ is the identity. We specialize to the case of rotation about the z-axis, which gives

$$\boldsymbol{R}(\theta) = \begin{bmatrix} \cos\theta & -\sin\theta & 0 \\ \sin\theta & \cos\theta & 0 \\ 0 & 0 & 1 \end{bmatrix}. \tag{28}$$

The total structural velocities and accelerations may be computed as

$$\frac{\partial \boldsymbol{u}}{\partial t} = \dot{\boldsymbol{u}} = \dot{\boldsymbol{u}}_\theta + \dot{\boldsymbol{u}}_d = \dot{\boldsymbol{R}}(\theta)(\boldsymbol{X} - \boldsymbol{X}_0) + \dot{\boldsymbol{u}}_d, \tag{29}$$

$$\frac{\partial^2 \boldsymbol{u}}{\partial t^2} = \ddot{\boldsymbol{u}} = \ddot{\boldsymbol{u}}_\theta + \ddot{\boldsymbol{u}}_d = \ddot{\boldsymbol{R}}(\theta)(\boldsymbol{X} - \boldsymbol{X}_0) + \ddot{\boldsymbol{u}}_d, \tag{30}$$

where

$$\dot{\boldsymbol{R}}(\theta) = \begin{bmatrix} -\sin\theta & -\cos\theta & 0 \\ \cos\theta & -\sin\theta & 0 \\ 0 & 0 & 0 \end{bmatrix} \dot{\theta}, \tag{31}$$

$$\ddot{\boldsymbol{R}}(\theta) = \begin{bmatrix} -\cos\theta & \sin\theta & 0 \\ -\sin\theta & -\cos\theta & 0 \\ 0 & 0 & 0 \end{bmatrix} \dot{\theta}^2 + \begin{bmatrix} -\sin\theta & -\cos\theta & 0 \\ \cos\theta & -\sin\theta & 0 \\ 0 & 0 & 0 \end{bmatrix} \ddot{\theta}. \tag{32}$$

In what follows, this decomposition of the structural displacement will be employed to define the motion of the fluid domain and to modify time integration procedures for the structural equations of motion.

2.3. Motion of the fluid domain

In the ALE framework the fluid domain moves to accommodate the structural motion. To ensure a smooth evolution of the fluid domain, we employ equations of linear elasticity to compute the fluid domain displacement [21–25]. The linear elastic equations are driven by the time-dependent displacement of the fluid-structure interface. In the discrete setting this procedure is referred to as mesh motion.

The present application is dominated by the rotation. However, large rotations are not in the kernel of the linear elasticity operator (i.e. large rotations generate stresses in the linear elastic framework). As a result, the direct application of linear elastostatics to compute the fluid domain motion may lead to undesired fluid mesh distortion, especially for long time integration. To circumvent this potential difficulty, we propose to decompose the fluid domain motion into rotation and deflection to handle the rotation exactly, and to employ linear elastostatics only for the deflection.

We introduce the total fluid domain displacement, $\boldsymbol{u}^m$,

$$\boldsymbol{u}^m = \boldsymbol{u}^m_\theta + \boldsymbol{u}^m_d, \tag{33}$$

where

$$\boldsymbol{u}^m_\theta = (\boldsymbol{R}(\theta) - \boldsymbol{I})\,(\boldsymbol{X} - \boldsymbol{X}_0) \tag{34}$$

is the fluid domain displacement associated with rotation about a fixed point $\boldsymbol{X}_0$. The fluid domain deflection may be computed from the following variational problem: Find $\boldsymbol{u}^m_d(t) \in \mathcal{V}^m$, such that $\forall \boldsymbol{w}^m \in \mathcal{W}^m$,

$$B^m\left(\boldsymbol{w}^m, \boldsymbol{u}^m_d(t)\right) - F^m\left(\boldsymbol{w}^m\right) = 0, \tag{35}$$

where the argument t is used to denote deflection at the current time. In Eq. (35)

$$B^m(\boldsymbol{w}, \boldsymbol{u}) = (\nabla^s_{\tilde{x}} \boldsymbol{w}, 2\mu^m \nabla^s_{\tilde{x}} \boldsymbol{u} + \lambda^m \nabla_{\tilde{x}} \cdot \boldsymbol{u} \boldsymbol{I})_{\Omega^f_{\tilde{t}}} \tag{36}$$

is the linear elasticity operator defined on the "nearby configuration" $\Omega^f_{\tilde{t}}$ taken at time $\tilde{t} < t$, and

$$F^m\left(\boldsymbol{w}^m\right) = B^m\left(\boldsymbol{w}^m, \boldsymbol{u}^m_d(\tilde{t})\right), \tag{37}$$

where $\boldsymbol{u}^m_d(\tilde{t})$ is considered known. The configuration $\Omega^f_{\tilde{t}}$ is obtained by rotating the fluid domain to current time t and deflecting to $\tilde{t}$, namely,

$$\Omega^f_{\tilde{t}} = \{\tilde{\boldsymbol{x}} \mid \tilde{\boldsymbol{x}} = \boldsymbol{X} + \boldsymbol{u}^m_\theta(t) + \boldsymbol{u}^m_d(\tilde{t})\}. \tag{38}$$

In practice, $\tilde{t} = t^n$, that is, in the definition of $\Omega^f_{\tilde{t}}$, the deflection is taken at the previous time step.

The total fluid domain displacement at time t is now computed as

$$\boldsymbol{u}^m(t) = \boldsymbol{u}^m_\theta(t) + \boldsymbol{u}^m_d(t), \tag{39}$$

and the fluid domain configuration at t becomes

$$\Omega^f_t = \{\boldsymbol{x} \mid \boldsymbol{x} = \boldsymbol{X} + \boldsymbol{u}^m(t)\}. \tag{40}$$

Remark: The pure rotation case is recovered by setting $\boldsymbol{u}^m_d = \boldsymbol{0}$. Likewise, the pure deflection case is recovered by setting $\boldsymbol{u}^m_\theta = \boldsymbol{0}$.

Remark: As an alternative to the proposed approach, nonlinear elasticity with an objective measure of strain may be used to compute the fluid domain motion. This, however, introduces an additional level of nonlinearity into the problem.

Remark: If the thin boundary-layer elements become even thinner during the computation or as a result of mesh refinement, it might be advantageous to stiffen those elements in a more direct way, such as by using the Solid-Extension Mesh Moving Technique (SEMMT), which was introduced in [26] and tested in [27] and [18].

2.4. Coupled problem

Given the individual subproblems, the weak formulation for the coupled FSI problem is stated as follows: Find $\{\boldsymbol{v}, p\} \in \mathcal{V}^f$, $\boldsymbol{u} \in \mathcal{V}^s$ and $\boldsymbol{u}^m_d \in \mathcal{V}^m$ such that $\forall\{\boldsymbol{w}^f, q^f\} \in \mathcal{W}^f$, $\forall \boldsymbol{w}^s \in \mathcal{W}^s$ and $\forall \boldsymbol{w}^m \in \mathcal{W}^m$,

$$\begin{aligned} B^f\left(\{\boldsymbol{w}^f, q^f\}, \{\boldsymbol{v}, p\}; \boldsymbol{v}^m\right) - F^f\left(\{\boldsymbol{w}^f, q^f\}\right) + B^s\left(\boldsymbol{w}^s, \boldsymbol{u}\right) - F^s\left(\boldsymbol{w}^s\right) \\ + B^m\left(\boldsymbol{w}^m, \boldsymbol{u}^m_d\right) - F^m\left(\boldsymbol{w}^m\right) = 0. \end{aligned} \tag{41}$$

In the above weak formulation the solution fields and weighting functions are chosen to ensure strong kinematic and weak traction coupling at the fluid-structure interface (see [25] for details).

3. Discrete solution procedures

In this section we briefly summarize our space discretization approach of the coupled FSI problem given by Eq. (41). We also present an adaptation of a class of time integration procedures for structures dominated by large rotational motions.

The solid and fluid mesh motion equations are discretized using the Galerkin approach. The fluid formulation makes use of the residual-based variational multiscale method [28, 29], which was presented in detail for moving domain problems in Part 1 of this paper. The coupled FSI equations are advanced in time using the Generalized-alpha method (see [25, 30, 31]). Within each time step, the coupled equations are solved using an inexact Newton approach. For every Newton iteration the following steps are performed: 1. We obtain the fluid solution increment holding the structure and mesh fixed; 2. We update the fluid solution, compute the aerodynamic force on the structure and compute the structural solution increment. The aerodynamic force at control points or nodes is computed using the conservative definition given in Part 1 of this paper; 3. We update the structural solution and use elastic mesh motion to update the fluid domain velocity and position. We recall that only the deflection part of the mesh motion is computed using linear elastostatics, while the rotation part is computed exactly. This three-step iteration is repeated until convergence to an appropriately coupled discrete solution is achieved. The proposed approach, also referred to as "block-iterative" (see [18] for the terminology), is stable because the wind turbine blades are relatively heavy structures.

Remark: Because the structural nonlinearity is stronger than that of the fluid, it may be beneficial to take additional inner iterations on the structure to improve its convergence.

In the proposed FSI framework the fluid and structural solves are decoupled. This gives us the flexibility of adjusting the structure time integration procedures to better capture the important features of the solution. In particular, we note that the bulk of the structural displacement comes from rotation of the blades about the horizontal axis. To better approximate rotation we separate the structure nodal or control point degrees of freedom into rotation and deflection as follows. Let $\boldsymbol{U}$, $\dot{\boldsymbol{U}}$ and $\ddot{\boldsymbol{U}}$ be the vectors of nodal or control point displacements, velocities and accelerations, respectively. We set

$$\boldsymbol{U} = \boldsymbol{U}_\theta + \boldsymbol{U}_d, \tag{42}$$

$$\dot{\boldsymbol{U}} = \dot{\boldsymbol{U}}_\theta + \dot{\boldsymbol{U}}_d, \tag{43}$$

$$\ddot{\boldsymbol{U}} = \ddot{\boldsymbol{U}}_\theta + \ddot{\boldsymbol{U}}_d, \tag{44}$$

where $\boldsymbol{U}_\theta$, $\dot{\boldsymbol{U}}_\theta$ and $\ddot{\boldsymbol{U}}_\theta$ are given by

$$\boldsymbol{U}_\theta = (\boldsymbol{R}(\theta) - \boldsymbol{I})\,(\boldsymbol{X} - \boldsymbol{X}_0), \tag{45}$$

$$\dot{\boldsymbol{U}}_\theta = \dot{\boldsymbol{R}}(\theta)(\boldsymbol{X} - \boldsymbol{X}_0), \tag{46}$$

$$\ddot{\boldsymbol{U}}_\theta = \ddot{\boldsymbol{R}}(\theta)(\boldsymbol{X} - \boldsymbol{X}_0). \tag{47}$$

The above Eqs. (45)-(47) present an exact relationship between the nodal or control point displacements, velocities and accelerations corresponding to the rotation. To relate the deflection degrees of freedom between time levels t_n and t_{n+1}, we make use of the standard Newmark formulas [32]

$$\dot{\boldsymbol{U}}_d^{n+1} = \dot{\boldsymbol{U}}_d^n + \Delta t \left((1-\gamma)\ddot{\boldsymbol{U}}_d^n + \gamma \ddot{\boldsymbol{U}}_d^{n+1} \right), \tag{48}$$

$$\boldsymbol{U}_d^{n+1} = \boldsymbol{U}_d^n + \Delta t \dot{\boldsymbol{U}}_d^n + \frac{\Delta t^2}{2} \left((1-2\beta)\ddot{\boldsymbol{U}}_d^n + 2\beta \ddot{\boldsymbol{U}}_d^{n+1} \right), \tag{49}$$

where γ and β are the time integration parameters chosen to maintain second-order accuracy and unconditional stability of the method, and $\Delta t = t_{n+1} - t_n$ is the time step size.

Combining exact rotations given by Eqs. (45)-(47) and time-discrete deflections given by Eqs. (48)-(49), we obtain the following modified Newmark formulas for the total discrete solution:

$$\begin{aligned} \dot{\boldsymbol{U}}^{n+1} = & \left\{ \dot{\boldsymbol{R}}^{n+1} - \left[\dot{\boldsymbol{R}}^n + \Delta t \left((1-\gamma)\ddot{\boldsymbol{R}}^n + \gamma \ddot{\boldsymbol{R}}^{n+1} \right) \right] \right\} (\boldsymbol{X} - \boldsymbol{X}_0) \\ & + \dot{\boldsymbol{U}}^n + \Delta t \left((1-\gamma)\ddot{\boldsymbol{U}}^n + \gamma \ddot{\boldsymbol{U}}^{n+1} \right), \end{aligned} \tag{50}$$

$$\begin{aligned} \boldsymbol{U}^{n+1} = & \left\{ \boldsymbol{R}^{n+1} - \left[\boldsymbol{R}^n + \Delta t \dot{\boldsymbol{R}}^n + \frac{\Delta t^2}{2} \left((1-2\beta)\ddot{\boldsymbol{R}}^n + 2\beta \ddot{\boldsymbol{R}}^{n+1} \right) \right] \right\} (\boldsymbol{X} - \boldsymbol{X}_0) \\ & + \boldsymbol{U}^n + \Delta t \dot{\boldsymbol{U}}^n + \frac{\Delta t^2}{2} \left((1-2\beta)\ddot{\boldsymbol{U}}^n + 2\beta \ddot{\boldsymbol{U}}^{n+1} \right). \end{aligned} \tag{51}$$

We employ Eqs. (50)-(51), in conjunction with the Generalized-alpha method, for the time discretization of the structure.

Remark: In the case of no rotation, for which $\boldsymbol{R}$ is an identity tensor, Eqs. (50) and (51) reduce to the standard Newmark formulas. In the case of no deflection, pure rotation is likewise recovered.

4. Simulation of the NREL 5MW offshore baseline wind turbine rotor

The wind turbine rotor is simulated at prescribed steady inlet wind velocity of 11.4 m/s and rotor angular velocity of 12.1 rpm. This setup corresponds to one of the cases reported in [19]. The problem setup is illustrated in Figure 2. The dimensions of the problem domain and the NURBS mesh employed are the same as in Part 1 of this paper. The air density and viscosity are set to 1.2 kg/m^3 and 2.0×10^{-5} kg/(m·s), respectively. The time step is chosen to be $\Delta t = 0.0003$ s.

As in Part 1, rotationally-periodic boundary conditions for the fluid are imposed in order to reduce computational cost. However, because the rotor blades are subject to gravity forces, a fully rotationally-periodic structural solution is not expected

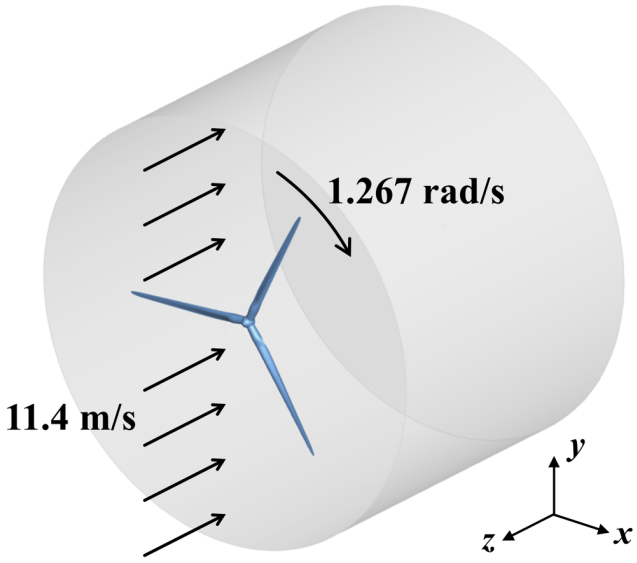

Figure 2: Problem setup.

in this case. Nevertheless, we feel that the use of rotationally-periodic boundary conditions for the fluid domain is justified due to the fact that the fluid periodic boundaries are located sufficiently far away from the structure and are not expected to affect the structural response. We note that rotationally periodic boundary conditions were employed earlier in [33, 34] for parachute simulations.

A symmetric fiberglass/epoxy composite with $[\pm 45/0/90_2/0_3]_s$ lay-up, which enhances flap-wise and edge-wise stiffness is considered for the rotor blade material. The 0° fiber points in the direction of a tangent vector to the airfoil cross-section curve. The orthotropic elastic moduli for each ply are given in Table 1. For simplicity, the entire blade is assumed to have the same lay-up. The resulting **A**, **B** and **D** matrices from Eqs. (18)-(20) are

$$\mathbf{A} = h \begin{bmatrix} 26.315 & 4.221 & 0 \\ 4.221 & 18.581 & 0 \\ 0 & 0 & 5.571 \end{bmatrix} \times 10^9 \,(\mathrm{N/m})\,, \tag{52}$$

$$\mathbf{B} = \mathbf{0}, \tag{53}$$

$$\mathbf{D} = h^3 \begin{bmatrix} 1.727 & 0.545 & 0.053 \\ 0.545 & 1.627 & 0.053 \\ 0.053 & 0.053 & 0.658 \end{bmatrix} \times 10^9 \,(\mathrm{N{\cdot}m})\,. \tag{54}$$

The total laminate thickness distribution is shown in Figure 3a. The blade shell model together with the bending strips covering the regions of C^0-continuity is shown in Figure 3b.

The computations are advanced in time until a statistically-stationary value of the aerodynamic torque is obtained. The rigid rotor under the same wind and ro-

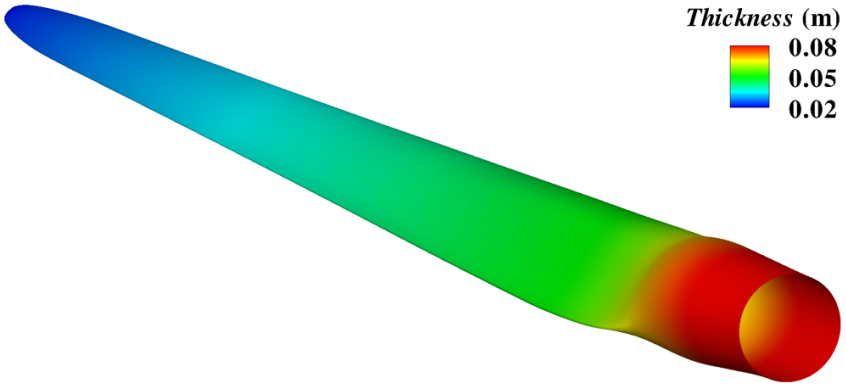

(a) Blade thickness

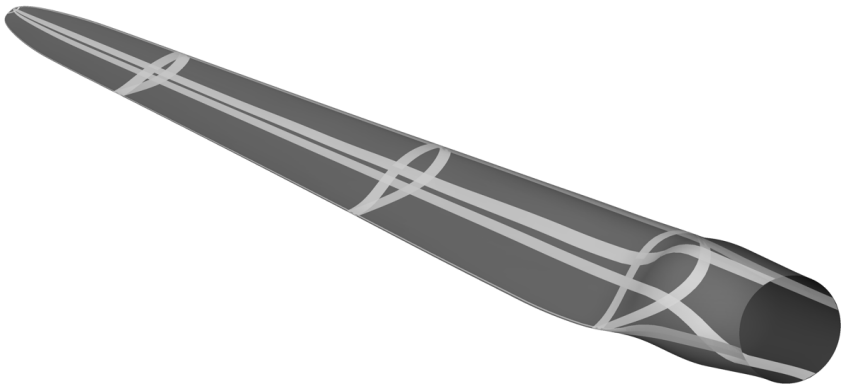

(b) Bending strips

Figure 3: NREL 5MW offshore baseline wind turbine rotor blade model.

E_1 (GPa)	E_2 (GPa)	G_{12} (GPa)	ν_{12} (–)	ρ (g/cm^3)
39	8.6	3.8	0.28	2.1

Table 1: Material properties of a unidirectional E-glass/epoxy composite taken from [35].

tor speed conditions is simulated for comparison. Contours of the pressure on the flexible blade in the current configuration are shown in Figure 4. The large negative pressure on the suction side creates a lift force vector with a component in the direction of the blade rotation, which generates a favorable aerodynamic torque.

The aerodynamic torque (for a single blade) is plotted in Figure 5 for both rigid and flexible blade simulations. Both cases compare favorably to the data reported in [19] for this setup obtained using FAST [36], which is a widely used software in wind turbine aerodynamics simulation. Computational modeling in FAST makes use of look-up tables to obtain steady-state lift and drag data for airfoil cross-sections and incorporates empirical modeling to account for the rotor hub, blade tips, and trailing-edge turbulence. In our simulations we are able to capture this

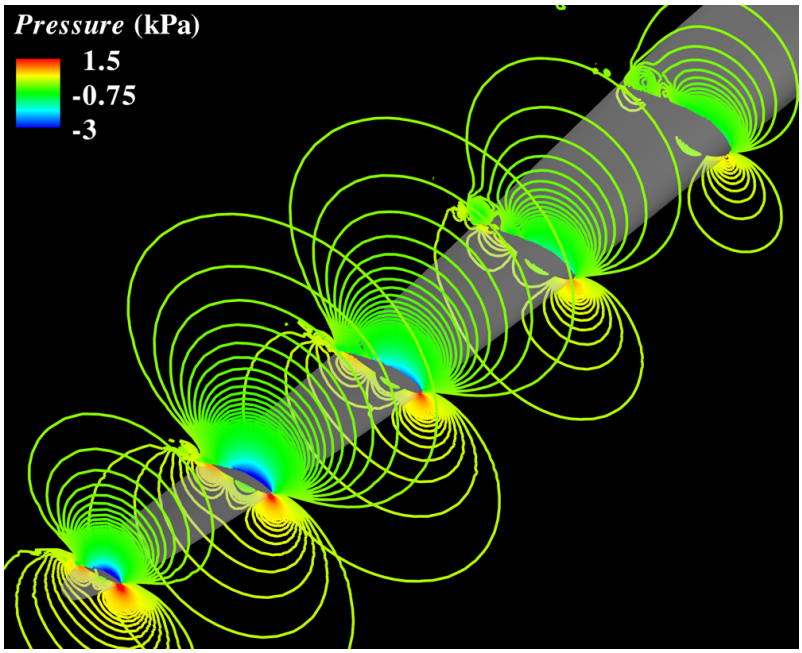

Figure 4: Pressure contours at several blade cross-sections at t = 0.7 s viewed from the back of the blade plotted on the deformed configuration. The large negative pressure at the suction side of the airfoil creates a favorable aerodynamic torque.

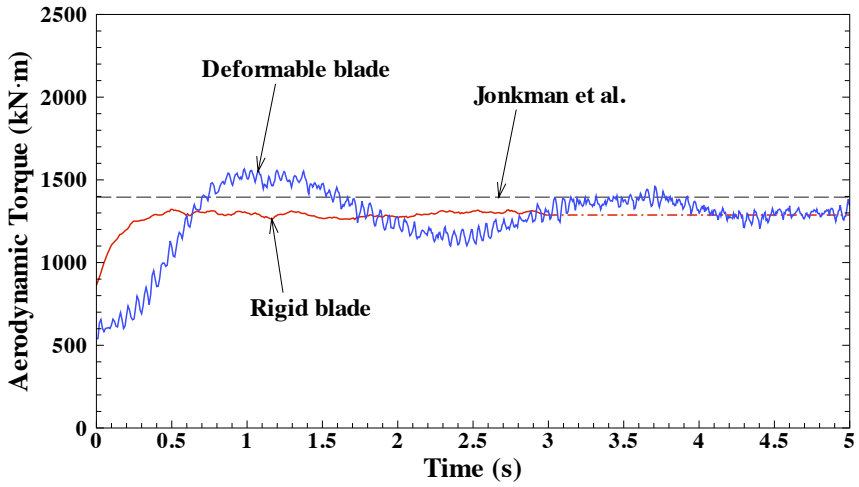

Figure 5: Time history of the aerodynamic torque. Both rigid and flexible rotor results are plotted. The reference steady-state result from [19] is also shown for comparison.

important quantity of interest using 3D FSI procedures, which do not rely on empiricism and are 100% predictive.

Rotor blade deflected shape at the point of maximum tip displacement is shown

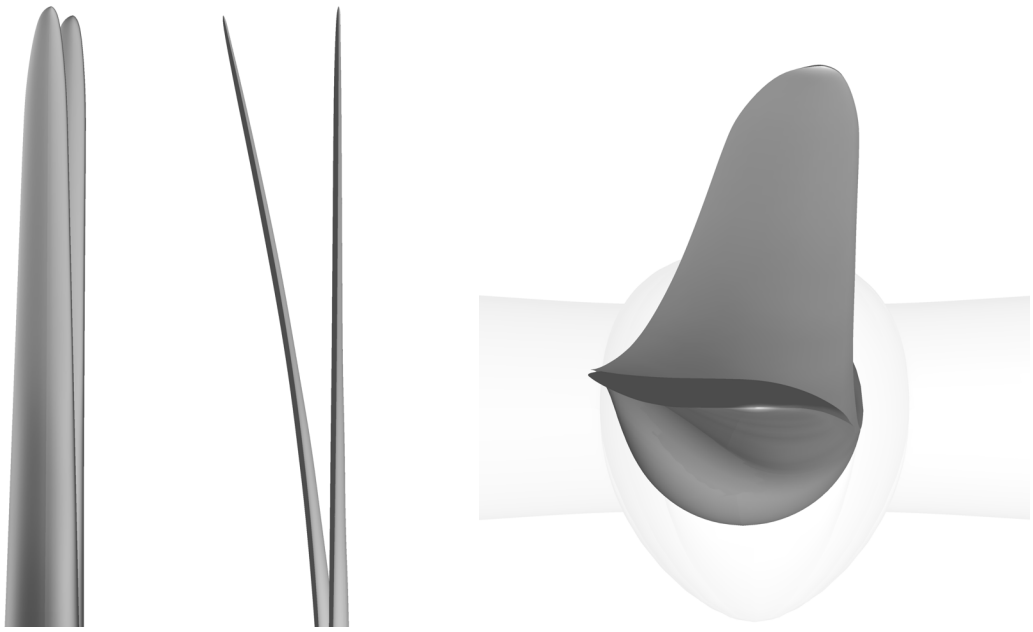

Figure 6: Rotor blade deflected shape at the point of maximum tip displacement. Front, side and top views are shown to better illustrate blade deflection characteristics.

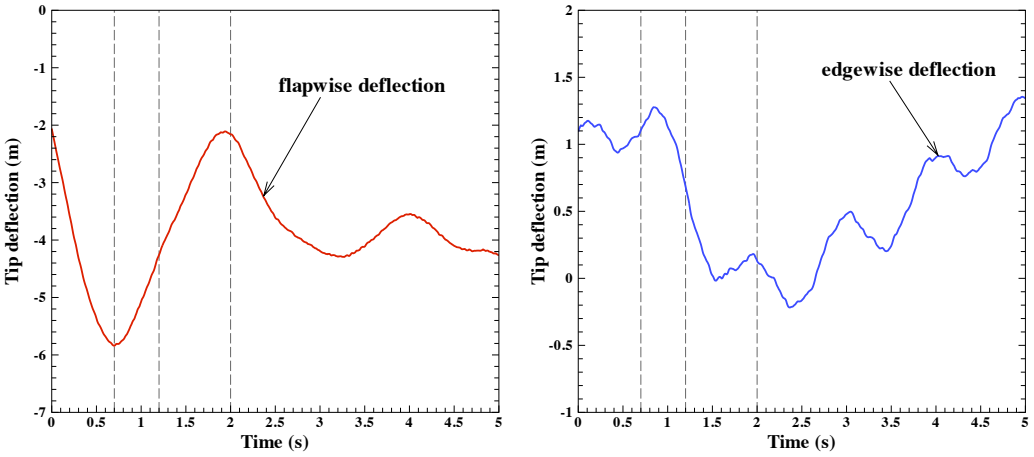

Figure 7: Time histories of the blade tip flap-wise (front-to-back) and edge-wise (side-to-side) deflection.

in Figure 6. As expected, the blade mostly displaces in the flap-wise direction, although some edge-wise deflection is also present. Time histories of the flap-wise and edge-wise displacements are shown in Figure 7. The maximum flap-wise tip deflection reaches nearly 6 m, which is significant, and is consistent with the data reported in [19]. There is a sudden decrease in the edge-wise deflection around

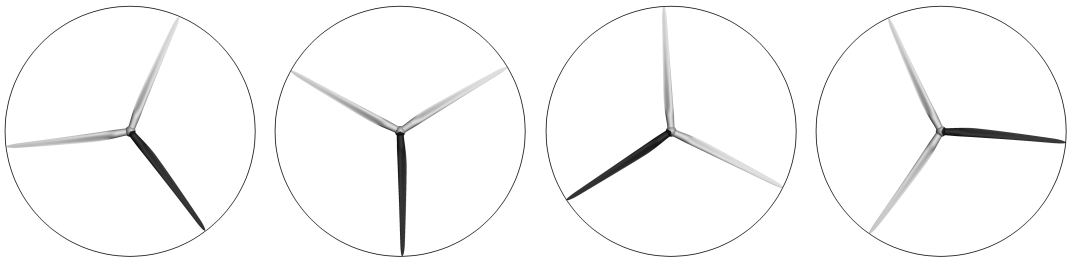

(a) t = 0.7 s (b) t = 1.2 s (c) t = 2.0 s (d) t = 5.0 s

Figure 8: Merged domain of the rotor configuration as several time instants during the simulation. The actual computational domain of the wind turbine rotor is highlighted using a darker shade.

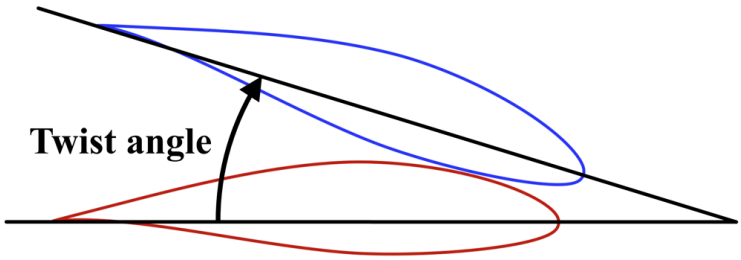

Figure 9: Definition of the blade cross-section twist angle.

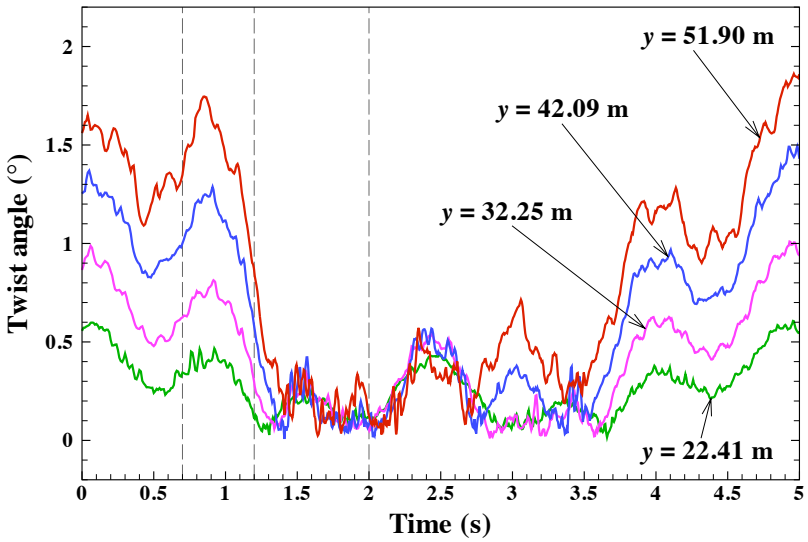

Figure 10: Time histories of the twist angle at four cross-sections along the blade axis.

t = 1.2 s. At that time the blade tip passes its lowest vertical position (see Figure 8 for blade location at different time instances) and the direction of the gravity force

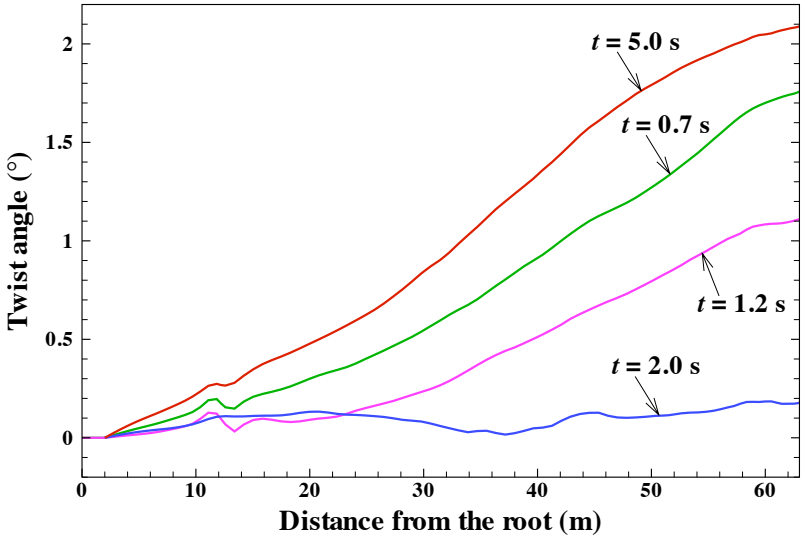

Figure 11: Distribution of the cross-section twist angle along the length of the blade at different time instances.

vector reverses with respect to the direction of the lift force vector.

Note that the aerodynamic torque for the flexible blade exhibits low-magnitude, high-frequency oscillations, while the rigid blade torque is smooth (see Figure 5). To better understand this behavior, we examine the twisting motion of the wind turbine blade about its axis. Figure 9 provides a definition of the twist angle for a given blade cross-section. Time histories of the twist angle at four different cross-sections are shown in Figure 10. The twist angle increases with distance from the root and reaches almost 2° near the tip in the early stages of the simulation. However, starting at $t = 1.2$ s, when the blade tip reaches its lowest vertical position, the magnitude of the twist angle is reduced significantly. The reversal of the gravity vector with respect to the lift direction clearly affects the edge-wise bending and twisting behavior of the blade. The blade twist angle undergoes high frequency oscillations, which are driven by the trailing-edge vortex shedding and turbulence. Local oscillations of the twist angle lead to the temporal fluctuations in the aerodynamic torque.

Remark: We note that in the computations presented here the structure is modeled as a shell with a smooth thickness variation. Structural members, such as spar caps and shear webs, which provide additional bending and torsional stiffness for improved blade response, are not considered here and will be added to the blade structural model in the future.

Figure 11 shows the blade cross-section twist angle as a function of cross-section distance from the root at different time instances. After the blade passes

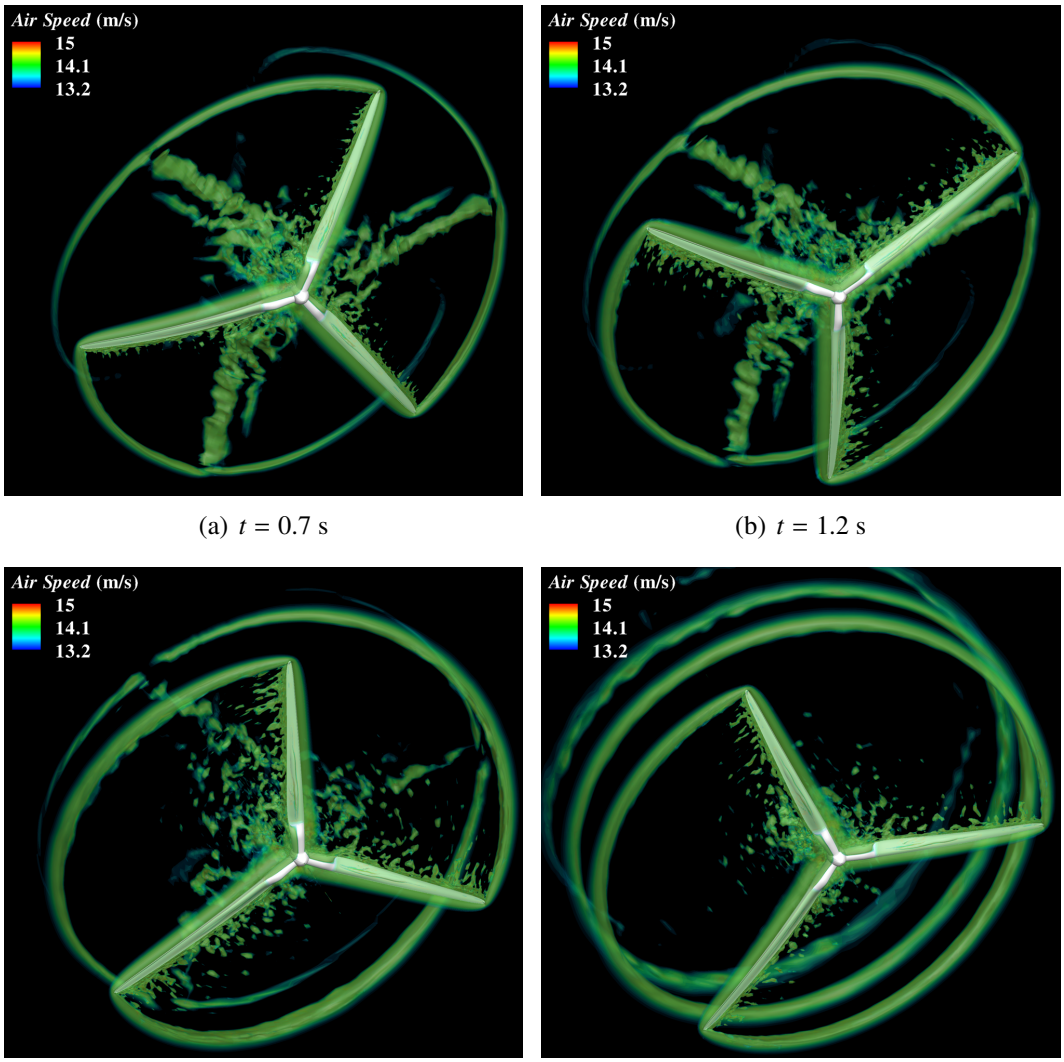

(a) $t = 0.7$ s (b) $t = 1.2$ s

(c) $t = 2.0$ s (d) $t = 5.0$ s

Figure 12: Isosurfaces of air speed at several instants in the simulation. The flow exhibits complex behavior. The vortical feature generated at the blade tip is convected downstream of the rotor with very little decay.

its lowest point, the distribution of the twist angle changes drastically.

Isosurfaces of the air speed at different time instances are shown in Figure 12. Note that, for visualization purposes the rotationally-periodic 120° domain was merged into a full 360° domain. Fine-grained turbulent structures are generated at the trailing edge of the blade along its entire length. The vortex forming at the tip of the blades is convected downstream of the rotor with little decay.

Figure 13 shows the isocontours of air speed at a planar cut superposed on the spinning rotor. Note the high-intensity turbulence in the blade aerodynamic zone,

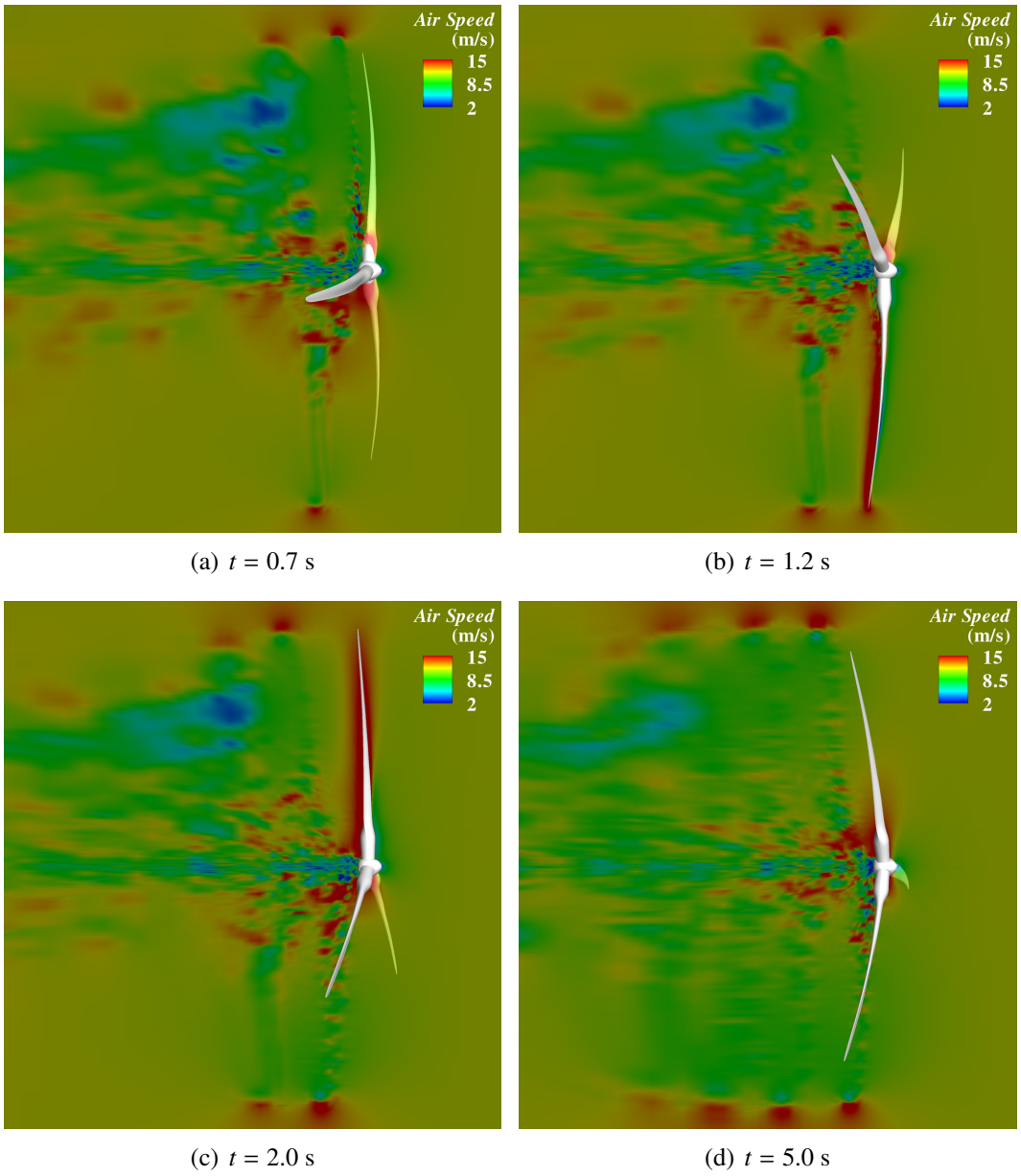

(a) $t = 0.7$ s (b) $t = 1.2$ s

(c) $t = 2.0$ s (d) $t = 5.0$ s

Figure 13: Isocontours of air speed at a planar cut superposed with the wind turbine rotor in the deformed configuration. Rotor blade deflection is clearly visible.

which is a segment of the blade where the cylindrical root rapidly transitions to a thin airfoil shape. This suggests that the blade trailing edge in this location is subjected to high-frequency loads that are fatiguing the blade. The blade displacement under the action of wind forces is also clearly visible.

Figure 14 shows the isocontours of relative wind speed at a 30 m radial cut at different time instances. For every snapshot the blade is rotated to the reference con-

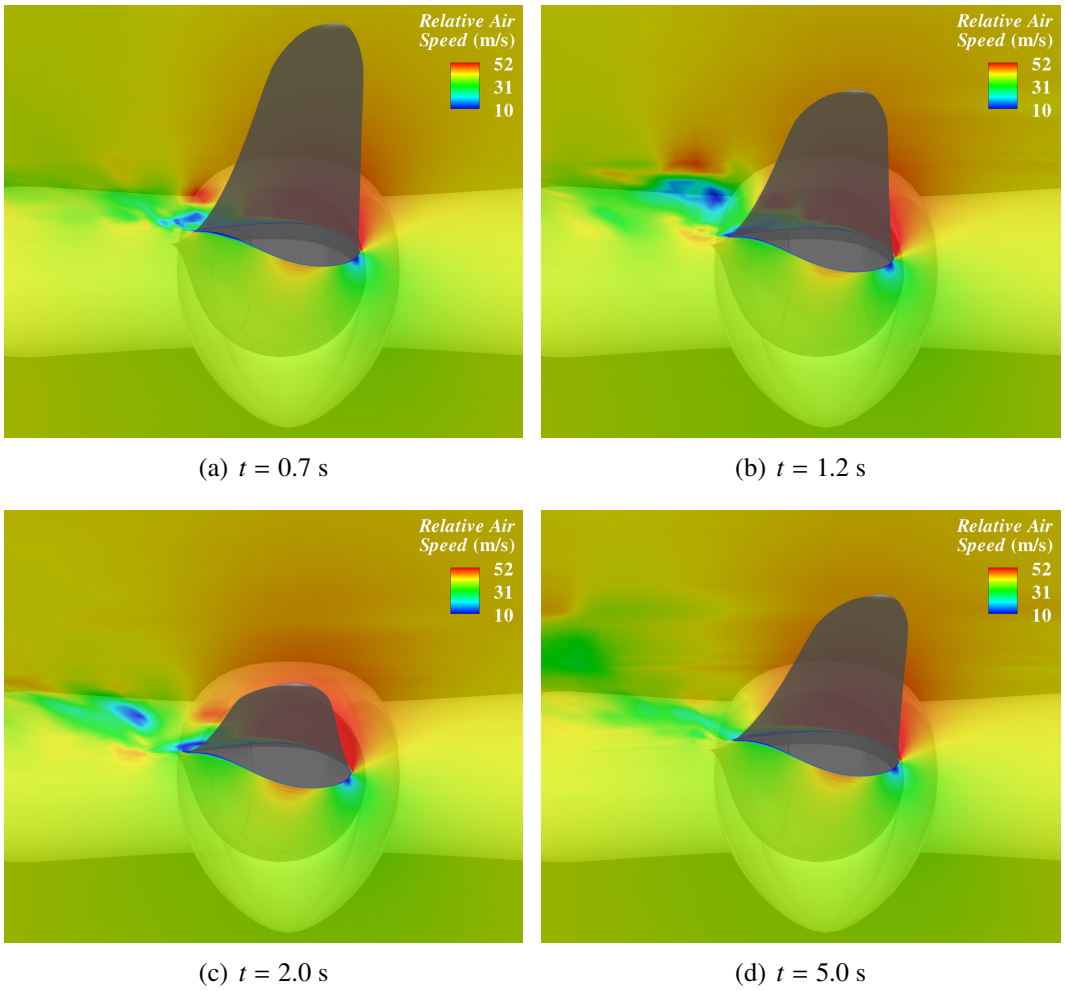

(a) $t = 0.7$ s (b) $t = 1.2$ s

(c) $t = 2.0$ s (d) $t = 5.0$ s

Figure 14: Isocontours of relative wind speed at a 30 m radial cut at different time instances superposed on a moving blade. The air flow is fully attached on the pressure side of the blade and separates on the suction side. The flow separation point varies as the blade moves under the action of wind, inertial, and gravitational forces.

figuration to better illustrate the deflection part of the motion. On the pressure side, the air flow boundary layer is attached to the blade for the entire cord length. On the suction side, the flow detaches near the trailing edge and transitions to turbulence.

At $t = 0.7$ s the composite blade experienced the maximum flap-wise tip deflection. We found the magnitudes of the stress components (in the basis corresponding to the material axes) for every ply are below the composite strength. The most critical stress component of the entire blade is σ_{22} in ply number 14 (0° fiber orientation). The maximum value of σ_{22} reaches 22.63 MPa, while the corresponding failure strength is 39 MPa [35]. This indicates the proposed blade design can withstand the simulated operating conditions. The isocontours of σ_{22} are plotted in Figure 15, and show strong tension on the front and compression on the back of the

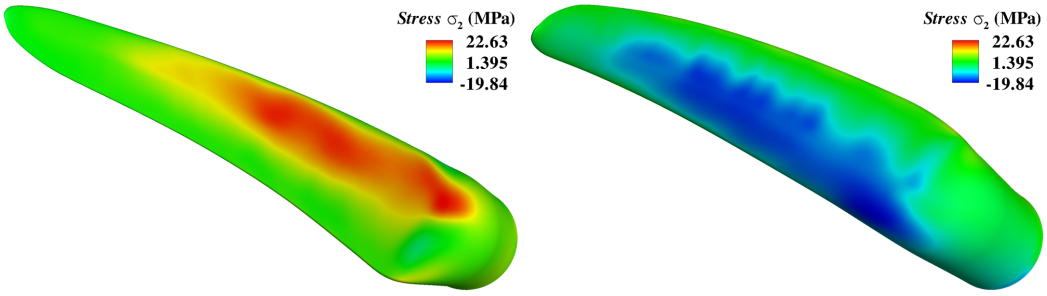

(a) (b)

Figure 15: Isocontours of stress component σ_{22} (in the direction transverse to the fiber) in the 14^{th} ply (0° fiber orientation) of the composite blade at $t = 0.7$ s view from the (a) front and (b) back of the blade. Strong tension on the front and compression on the back of the blade are found.

blade.

5. Conclusions

In this paper we presented our computational FSI procedures for the simulation of wind turbine rotors at full scale. The air flow is modeled using the residual-based variational multiscale formulation of turbulent flow and the structure is governed by the rotation-free Kirchhoff-Love shell theory with the aid of the bending strip method. NURBS-based isogeometric analysis is employed for spatial discretization. The fluid and solid are strongly coupled at their interface. The strong coupling is in part facilitated by the fact that the structure has only displacement degrees of freedom. The coupled system is solved in a block-iterative fashion, which is a robust procedure for the present application due to the relatively high structural mass of the wind turbine blades.

For wind turbine rotors the structural motion is dominated by rotation about the horizontal axis. For this we found it advantageous for overall accuracy of the computations to separate the structural displacement into rotation and deflection parts. With this decomposition, we modified the Newmark formulas to treat the rotation part of the structural motion exactly. In addition, only the deflection part of the mesh motion makes use of the partial differential equations of linear elastostatics, while the mesh rotation is computed exactly.

We applied our computational framework to the simulation of the NREL 5MW offshore baseline wind turbine rotor. The rotor blades are modeled as symmetric composite laminates homogenized in the through-thickness direction. The computational results give good prediction of the aerodynamic torque and blade tip deflection. To our knowledge, this is the first application of fully coupled FSI procedures to wind turbine rotor simulation at full scale.

This work is only a first step in the direction of FSI modeling of wind turbines. In the future, we plan to enhance our blade structural modeling to include spar caps,

shear webs, and other structural components not considered in this work.

We also feel the effect of the wind turbine tower is important. The presence of the tower will affect the aerodynamics and, consequently, wind loading on the blades. As a result, the rotor-tower interaction needs to be taken into account. For this, we plan to adopt procedures developed in [37] for the coupling of rotating and stationary domains that are particularly well suited for isogeometric discretizations.

In the long run, we plan to combine FSI and structural optimization to devise better blade designs and understand the sensitivity of power generation to changes in wind conditions, blade geometry and material properties.

Acknowledgement

We wish to thank the Texas Advanced Computing Center (TACC) at the University of Texas at Austin for providing HPC resources that have contributed to the research results reported within this paper. M.-C. Hsu was partially supported by the Los Alamos – UC San Diego Educational Collaboration Fellowship. The authors would like to acknowledge the funding of the International Graduate School of Science and Engineering (IGSSE) at Technische Universität München. This support is gratefully acknowledged.

References

[1] C. Tongchitpakdee, S. Benjanirat, and L.N. Sankar. Numerical simulation of the aerodynamics of horizontal axis wind turbines under yawed flow conditions. *Journal of Solar Energy Engineering*, 127:464–474, 2005.

[2] N. Sezer-Uzol and L.N. Long. 3-D time-accurate CFD simulations of wind turbine rotor flow fields. *AIAA Paper 2006-0394*, 2006.

[3] F. Zahle and N.N. Sørensen. Overset grid flow simulation on a modern wind turbine. *AIAA Paper 2008-6727*, 2008.

[4] F. Zahle, N.N. Sørensen, and J. Johansen. Wind turbine rotor-tower interaction using an incompressible overset grid method. *Wind Energy*, 12:594–619, 2009.

[5] E. Guttierez, S. Primi, F. Taucer, P. Caperan, D. Tirelli, J. Mieres, I. Calvo, J. Rodriguez, F. Vallano, G. Galiotis, and D. Mouzakis. A wind turbine tower design based on fibre-reinforced composites. Technical report, Joint Research Centre - Ispra, European Laboratory for Structural Assessment (ELSA), Institute For Protection and Security of the Citizen (IPSC), European Commission, 2003.

[6] C. Kong, J. Bang, and Y. Sugiyama. Structural investigation of composite wind turbine blade considering various load cases and fatigue life. *Energy*, 30:2101–2114, 2005.

[7] M.O.L. Hansen, J.N. Sørensen, S. Voutsinas, N. Sørensen, and H.Aa. Madsen. State of the art in wind turbine aerodynamics and aeroelasticity. *Progress in Aerospace Sciences*, 42:285–330, 2006.

[8] F.M. Jensen, B.G. Falzon, J. Ankersen, and H. Stang. Structural testing and numerical simulation of a 34 m composite wind turbine blade. *Composite Structures*, 76:52–61, 2006.

[9] T.J.R. Hughes, J.A. Cottrell, and Y. Bazilevs. Isogeometric analysis: CAD, finite elements, NURBS, exact geometry and mesh refinement. *Computer Methods in Applied Mechanics and Engineering*, 194:4135–4195, 2005.

[10] Y. Bazilevs, M.-C. Hsu, I. Akkerman, S. Wright, K. Takizawa, B. Henicke, T. Spielman, and T.E. Tezduyar. 3D simulation of wind turbine rotors at full scale. Part I: Geometry modeling and aerodynamics. *International Journal for Numerical Methods in Fluids*, 2010. Published online, doi:10.1002/fld.2400.

[11] J. Kiendl, Y. Bazilevs, M.-C. Hsu, R. Wüchner, and K.-U. Bletzinger. The bending strip method for isogeometric analysis of Kirchhoff–Love shell structures comprised of multiple patches. *Computer Methods in Applied Mechanics and Engineering*, 199:2403–2416, 2010.

[12] J. Kiendl, K.-U. Bletzinger, J. Linhard, and R. Wüchner. Isogeometric shell analysis with Kirchhoff–Love elements. *Computer Methods in Applied Mechanics and Engineering*, 198:3902–3914, 2009.

[13] Y. Bazilevs, V.M. Calo, J.A. Cottrell, J.A. Evans, T.J.R. Hughes, S. Lipton, M.A. Scott, and T.W. Sederberg. Isogeometric analysis using T-splines. *Computer Methods in Applied Mechanics and Engineering*, 199:264–275, 2010.

[14] M.R. Dörfel, B. Jüttler, and B. Simeon. Adaptive isogeometric analysis by local h-refinement with T-splines. *Computer Methods in Applied Mechanics and Engineering*, 199:264–275, 2010.

[15] F. Cirak, M. Ortiz, and P. Schröder. Subdivision surfaces: a new paradigm for thin shell analysis. *International Journal for Numerical Methods in Engineering*, 47:2039–2072, 2000.

[16] F. Cirak and M. Ortiz. Fully C^1-conforming subdivision elements for finite deformation thin shell analysis. *International Journal for Numerical Methods in Engineering*, 51:813–833, 2001.

[17] F. Cirak, M. J. Scott, E. K. Antonsson, M. Ortiz, and P. Schröder. Integrated modeling, finite-element analysis, and engineering design for thin-shell structures using subdivision. *Computer-Aided Design*, 34:137–148, 2002.

[18] T.E. Tezduyar, S. Sathe, R. Keedy, and K. Stein. Space–time finite element techniques for computation of fluid–structure interactions. *Computer Methods in Applied Mechanics and Engineering*, 195:2002–2027, 2006.

[19] J. Jonkman, S. Butterfield, W. Musial, and G. Scott. Definition of a 5-MW reference wind turbine for offshore system development. Technical Report NREL/TP-500-38060, National Renewable Energy Laboratory, Golden, CO, 2009.

[20] J.N. Reddy. *Mechanics of Laminated Composite Plates and Shells: Theory and Analysis, 2nd ed.* CRC Press, Boca Raton, FL, 2004.

[21] T.E. Tezduyar, M. Behr, S. Mittal, and A.A. Johnson. Computation of unsteady incompressible flows with the finite element methods – space–time formulations, iterative strategies and massively parallel implementations. In *New Methods in Transient Analysis*, PVP-Vol.246/AMD-Vol.143, pages 7–24, New York, 1992. ASME.

[22] T. Tezduyar, S. Aliabadi, M. Behr, A. Johnson, and S. Mittal. Parallel finite element computation of 3D flows. *Computer*, 26:27–36, 1993.

[23] A.A. Johnson and T.E. Tezduyar. Mesh update strategies in parallel finite element computations of flow problems with moving boundaries and interfaces. *Computer Methods in Applied Mechanics and Engineering*, 119:73–94, 1994.

[24] Y. Bazilevs, V.M. Calo, Y. Zhang, and T.J.R. Hughes. Isogeometric fluid-structure interaction analysis with applications to arterial blood flow. *Computational Mechanics*, 38:310–322, 2006.

[25] Y. Bazilevs, V.M. Calo, T.J.R. Hughes, and Y. Zhang. Isogeometric fluid-structure interaction: theory, algorithms, and computations. *Computatonal Mechanics*, 43:3–37, 2008.

[26] T.E. Tezduyar. Finite element methods for fluid dynamics with moving boundaries and interfaces. In E. Stein, R. de Borst, and T.J.R. Hughes, editors, *Encyclopedia of Computational Mechanics, Vol. 3, Fluids*, chapter 17. Wiley, 2004.

[27] K. Stein, T.E. Tezduyar, and R. Benney. Automatic mesh update with the solid-extension mesh moving technique. *Computer Methods in Applied Mechanics and Engineering*, 193:2019–2032, 2004.

[28] Y. Bazilevs, V.M. Calo, J.A. Cottrel, T.J.R. Hughes, A. Reali, and G. Scovazzi. Variational multiscale residual-based turbulence modeling for large eddy simulation of incompressible flows. *Computer Methods in Applied Mechanics and Engineering*, 197:173–201, 2007.

[29] Y. Bazilevs and I. Akkerman. Large eddy simulation of turbulent Taylor–Couette flow using isogeometric analysis and the residual–based variational multiscale method. *Journal of Computational Physics*, 229:3402–3414, 2010.

[30] K. E. Jansen, C. H. Whiting, and G. M. Hulbert. A generalized-α method for integrating the filtered Navier-Stokes equations with a stabilized finite element method. *Computer Methods in Applied Mechanics and Engineering*, 190:305–319, 1999.

[31] J. Chung and G. M. Hulbert. A time integration algorithm for structural dynamics with improved numerical dissipation: The generalized-α method. *Journal of Applied Mechanics*, 60:371–75, 1993.

[32] T. J. R. Hughes. *The finite element method: Linear static and dynamic finite element analysis*. Prentice Hall, Englewood Cliffs, NJ, 1987.

[33] K. Takizawa, C. Moorman, S. Wright, T. Spielman, and T.E. Tezduyar. Fluid–structure interaction modeling and performance analysis of the Orion spacecraft parachutes. *International Journal for Numerical Methods in Fluids*, 2010. Published online, doi:10.1002/d.2348.

[34] K. Takizawa, S. Wright, C. Moorman, and T.E. Tezduyar. Fluid–structure interaction modeling of parachute clusters. *International Journal for Numerical Methods in Fluids*, 2010. Published online, doi:10.1002/d.2359.

[35] I.M. Daniel and O. Ishai. *Engineering Mechanics of Composite Materials*. Oxford University Press, New York, NY, 1994.

[36] J.M. Jonkman and M.L. Buhl Jr. FAST user's guide. Technical Report NREL/EL-500-38230, National Renewable Energy Laboratory, Golden, CO, 2005.

[37] Y. Bazilevs and T.J.R. Hughes. NURBS-based isogeometric analysis for the computation of flows about rotating components. *Computatonal Mechanics*, 43:143–150, 2008.